Journal of Japan Association for Earthquake Engineering, Vol. 25, No. 8, 2025

ON THE INTERACTION OF HORIZONTAL AND VERTICAL MOTION OBSERVED IN THE STRONG EARTHQUAKE RECORDS

Satoshi MORIO[1], Yoshinori KATO[2] and Tirawat BOONYATEE[3]

[1] Member, Dr. Eng., HAKUHO Architech Co., LTD. (Visiting Professor of Chulalongkorn University)
Mie, Japan, bonno51.krungtape@gmail.com
[2] Member, Dr. Eng., Professor, National Institute of Technology, Maizuru College
Kyoto, Japan, kato@maizuru-ct.ac.jp
[3] Ph.D., Associate Professor, Chulalongkorn University
Bangkok, Thailand, dr.tirawat@gmail.com

ABSTRACT: In the 2018 Hokkaido Eastern Iburi Earthquake (M6.7), seismic intensities as high as 7 and 6+ were observed at KiK-net Oiwake (IBUH01) and K-NET Oiwake (HKD127) stations, respectively. The large acceleration records observed at both stations are discussed based on constant-pressure cyclic direct box shear tests, microscopic studies, and elastoplastic theory. As a result, it was shown that at both observation points, downward vertical acceleration (volume expansion) occurred due to the dilatancy of the surface ground, and that the generated vertical and horizontal motions were strongly coupled.

Keywords: *Dilatancy, Vertical ground motion, Strong earthquake records, Coupling between vertical and horizontal ground motion*

1. INTRODUCTION

Morio et al.[1)] conducted a study on the strong earthquake records from the KiK-net Ichinoseki-W (IWTH25) station during the 2008 Iwate-Miyagi Nairiku Earthquake (M7.2), as well as the K-NET Tsukidate (MYG004) station during the 2011 off the Pacific Coast of Tohoku Earthquake (M9.0). In their study, vertically asymmetric strong acceleration records, with a maximum of 3866 gal (1 gal = 1 cm/s^2) at the Ichinoseki-W station, were simulated by an elastoplastic analysis using simultaneous input of horizontal and vertical motions. They demonstrated that when a large horizontal acceleration (shear) is applied simultaneously with an upward vertical acceleration (resulting in an increase in confining pressure), the stress point will rise along the failure line, resulting in further amplified upward vertical acceleration. Conversely, when a horizontal acceleration (shear) is applied while the downward vertical acceleration is close to −1 G (1 G = 980 gal) (resulting in a decrease in confining pressure), the stress point will decline along the failure line, leading to a strong plastic response under low confining pressure. Additionally, they suggested that the strong earthquake records at the Tsukidate station may include downward vertical acceleration caused by the dilatancy of shallow ground layers. They also demonstrated that the frequency of this vertical motion is twice that of the horizontal motion.

Furthermore, they pointed out that the large upward vertical acceleration at the Ichinoseki-W station may have been the result of the peak phase of upward vertical acceleration propagating from the lower layer overlapping with vertical acceleration of the same sign (upward) due to the dilatancy of surface layers.

Understanding the reasons behind the significantly strong seismic records is crucial for future earthquake motion predictions. This paper focuses on the analysis of such records at the KiK-net Oiwake (IBUH01) and K-NET Oiwake (HKD127) stations during the 2018 Hokkaido Eastern Iburi Earthquake, based on constant-pressure cyclic direct box shear test results, microscopic studies, and elastoplastic theory. Results from the study reveal that at both locations, there was a downward vertical acceleration (volumetric expansion) caused by the dilatancy of low-velocity surface layers. Moreover, the study demonstrates a strong coupling between the generated vertical and horizontal motions. The physical mechanism underlying the generation of these upward and downward accelerations and displacements will be discussed in Chapter 3. It can be understood that this phenomenon arises due to the reversible volumetric changes[2)–5)] inherent in granular materials.

2. STRONG GROUND MOTION (THE 2018 HOKKAIDO EASTERN IBURI EARTHQUAKE)

The Hokkaido Eastern Iburi Earthquake (M6.7), which struck on September 6th at 3:07 a.m., was caused by a steep reverse fault oriented in a north-south direction. Seismic intensity levels of 7 and 6+ were recorded at the KiK-net Oiwake (IBUH01) and the K-NET Oiwake (HKD127) stations, which are 100 meters apart[6)]. The focal depth, epicentral distance, and hypocentral distance to these stations are 37 km, 25.6 km, and 45 km, respectively. The take-off angle from the source to the site is quite high at 141°.

2.1 KiK-net Oiwake (IBUH01)

Figure 1 shows the acceleration waveforms at the ground surface of the KiK-net Oiwake (IBUH01) station. Table 1 summarizes the maximum accelerations at the borehole (GL−100.6 m) and at the ground surface, and the amplification factors, while Table 2 details the geological structure. Notably, the amplification factor for the vertical component in Table 1 is significantly large, at 12.6 times. Figure 2 shows the comparison between UD1 component at the borehole and UD2 component at the ground surface (from 8 to 12 s).

In Fig. 2, black straight lines indicate where the peaks of the UD1 and UD2 components align. Based on the separation distance (100.6 m) and the observed delay times, the average propagation speed is determined to be 1550 m/s. The waveform of UD2 is almost identical to that of UD1 until about 10 s, when strong amplification is observed in the NS2 component. However, from the latter half of 10 s, the characteristic of the waveform significantly changes. Among the phases marked with ●, ②, ④, ⑥, and ⑧ are peak phases of the UD2 component. As shown by the red line sloping downward to the right, there is no large peak phase of the UD1 component that corresponds to these peak phases. Similarly, the troughs marked by ①, ③, ⑤ and ⑦ are not proportional to those in the UD1 component. This discrepancy suggests that the signal during this period is influenced by additional factors compared to the earlier part.

Next, let us focus on the larger horizontal acceleration, NS component. Figure 3 exhibits the borehole acceleration (NS1) and the ground surface acceleration (NS2) between 9 to 13 s. As indicated by the black straight line, the phases of NS1 and NS2 approximately match until around 11 s. Based on the separation distance and observed delay times, an average propagation speed of 437 m/s can be determined. However, as the amplitude of horizontal acceleration increases after 11 s, the propagation velocities, as estimated from the red lines (drawn through points Ⓐ, Ⓑ, and Ⓒ), clearly decrease. These propagation velocities are 325 m/s, 224 m/s, and 190 m/s, respectively. Since the acceleration waveform exhibits intense variations, we also computed the propagation speeds from the velocity waveform, which yielded nearly identical results.

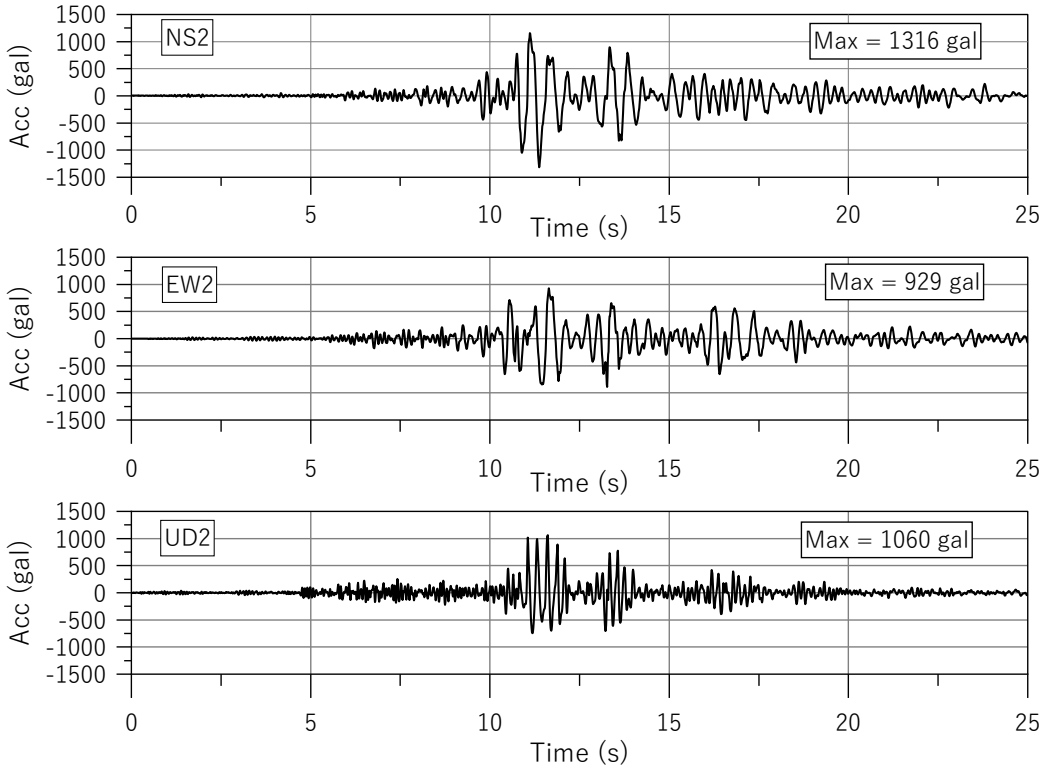

Fig. 1 Acceleration time history waveforms at the ground surface in KiK-net Oiwake (IBUH01)

Table 1 Maximum acceleration and amplification factor

Ground surface		Bore hole		Amplification factor
Component	(gal)	Component	(gal)	
NS2	1316	NS1	182	7.2
EW2	929	EW1	255	3.6
UD2	1060	UD1	84	12.6

Table 2 Underground structure at KiK-net Oiwake (IBUH01)

Thickness (m)	V_s (m/s)	V_p (m/s)	Depth (m)	Soil column
4	130	310		Silt
8	250	1300	11.0	
8	450	1870		Mud Stone
30	580	1870		
16	710	1870		
37.6	890	1870	103.6	
—	890	1870		

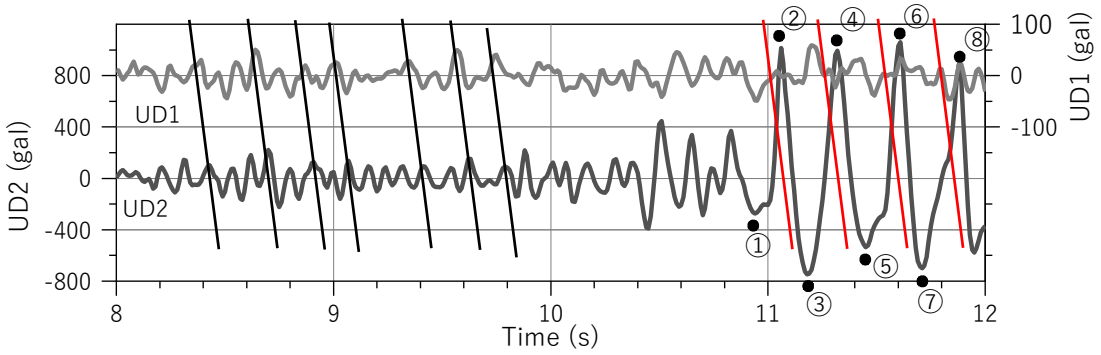

Fig. 2 Vertical acceleration waveforms at the ground surface (UD2) and at the borehole (UD1)

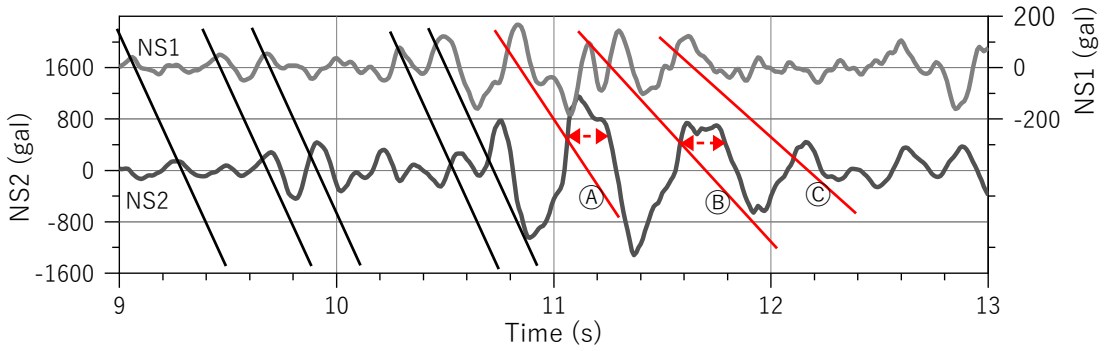

Fig. 3 Horizontal acceleration waveforms at the ground surface (NS2) and at the borehole (NS1)

Morio and Kato[7] utilized vertical array observation records at Port Island, during the Southern Hyogo Prefecture Earthquake, to determine the differences in the propagation speeds of P-waves and S-waves for the main shock and aftershocks. A similar technique is used to analyze the strong ground motions in Fig. 4. Based on spectral analysis of the signals, the phase spectrum as shown in Fig. 4 can be obtained. Note that the number of data points in the spectral analysis was 4096, and the Parzen window (bandwidth 0.8 Hz) was used as the spectrum window. As shown in Fig. 4(a), the phase spectrum of the UD component aligns with the red line, which represents a velocity of 1550 m/s. In Fig. 4(b), the phase spectrum of the NS component is plotted alongside that for a velocity of 437 m/s. Although the phase spectra in Fig. 4 closely align with the red lines, the coherence and cross-correlation functions of the analyzed signals are significantly lower than those observed in the Port Island study, particularly for the NS component. This discrepancy is likely due to the large inter-station distance with respect to the wavelength, and the strong transient characteristics of the waveform.

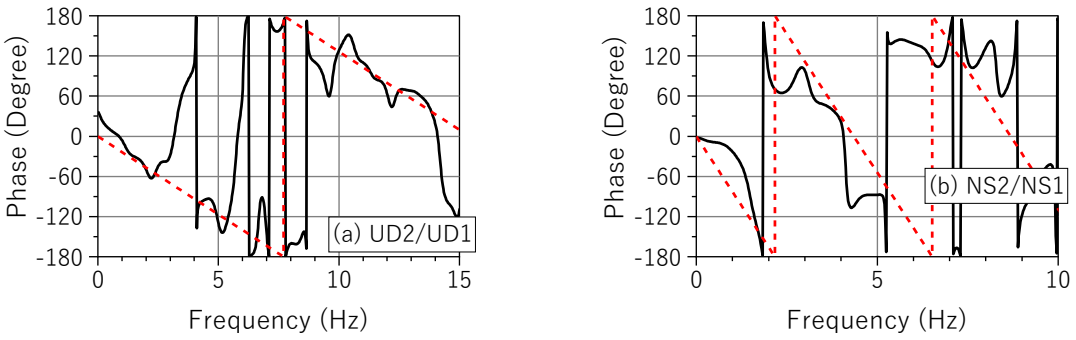

(a) UD2/UD1 (b) NS2/NS1

Fig. 4 Phase spectrum of UD and NS components between the ground surface and the borehole

Morio et al.[1] suggested that the strong ground motion recorded at the K-NET Tsukidate (MYG004) station during the 2011 off the Pacific Coast of Tohoku Earthquake was due to a transient resonance phenomenon. As shown in Fig. 3, as the dominant frequency of the surface layer decreased, it is believed that a resonance phenomenon occurred around 2 Hz, where the thickness of the surface soil layer corresponds to 1/4 of the wavelength, causing the amplitude of the NS2 component to increase.

Figure 5 shows the Fourier spectrum and spectral ratios for the UD and NS components. The NS component exhibits a significant amplification of 23 times around 1.8 Hz, while the UD component shows a magnification of 24 times around 4.1 Hz. For the UD component, an average velocity of 1550 m/s indicates that the 1/4 wavelength of the 3.85 Hz wave coincides with the burial depth of the borehole (GL−100.6 m). In other words, the extremely large amplification at 3 to 4 Hz is likely due to the phase cancellation of the ascending and descending waves[8].

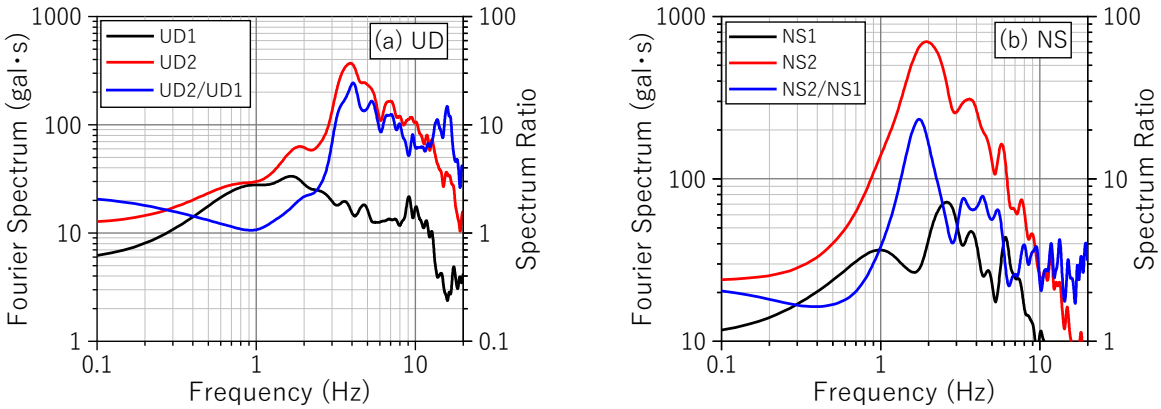

(a) UD component (b) NS component

Fig. 5 Fourier spectrum of UD and NS components and spectrum ratio

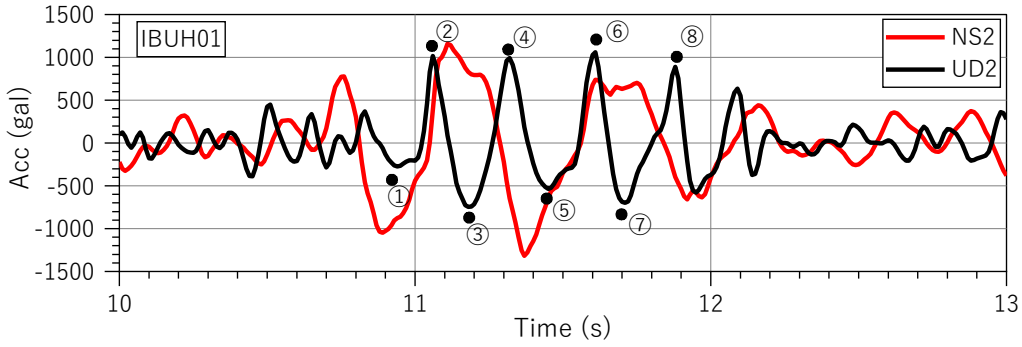

Fig. 6 Acceleration time history waveforms of UD2 and US2 components (IBUH01)

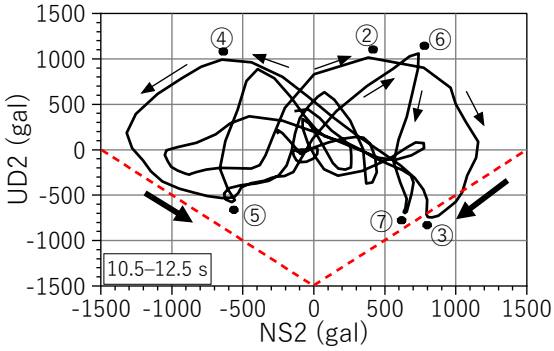

Fig. 7 Acceleration orbit of UD2 and NS2 components (IBUH01)

Figure 6 presents a combined time history of UD2 and NS2 components at the ground surface (from 10 to 13 s). In this figure, labels ①–⑧ correspond to the same locations as in Fig. 2. It is observed that the troughs of the UD2 component at ①, ③, ⑤, and ⑦ occur slightly after the extrema of the NS2 component. Figure 7 displays the acceleration orbit of the UD2 and NS2 components (from 10.5 to 12.5 s). This figure can be interpreted as a stress path diagram, where the UD2 and NS2 components represent the vertical normal stress σ_z and shear stress τ, respectively (see Appendix 1). For discussion purposes, failure lines are also schematically represented with red dashed lines in the same figure. When considering this diagram as a stress path, it is easier to understand if you think of it on a scale that adds gravitational acceleration of 1G (= 980 gal) to the vertical axis (see 3.5 below). Among the trough points

of the UD2 component, points ③ and ⑦ occur slightly after the peaks of the NS2 component, while points ① and ⑤ occur slightly after the troughs of the NS2 component. Additionally, the frequency of the UD motion (4 Hz) is approximately twice that of the horizontal motion (2 Hz), as shown in Fig. 5. The delay of the trough points in the UD2 motion relative to the extrema of the NS2 motion reflects a drop in the stress point along the failure line, moving toward the origin in the stress space.

Previous research[9] has discussed the phase characteristics (time delays) between horizontal and vertical motions during the Southern Hyogo Prefecture Earthquake. The frequency of the vertical motion will not ~~to~~ be twice that of the horizontal motion when SV waves arrive at an oblique angle.

Additionally, the K-NET Oiwake (HKD127) station, which will be discussed in the next section, and this observation point (IBUH01) are on the same slope ground (Kashiwaga Oka baseball field)[6] and did not exhibit this phenomenon during medium-sized earthquakes or aftershocks. The coupling between horizontal and vertical motions due to dilatancy has been observed in several strong earthquake records[10] considered to be on horizontal ground. It is unlikely that this phenomenon is due to the irregularity of the soil layer.

2.2 K-NET Oiwake (HKD127)

Figure 8 shows the time histories of the UD and EW components at the K-NET Oiwake (HKD127) station (from 11 to 13 s). The trough of the UD component at point ③ occurs slightly after the peak of the EW component, while the troughs at points ① and ⑤ occur slightly after the troughs of the EW component.

Figure 9 illustrates the acceleration orbit of the UD and EW components over the same time period. The dashed red lines in this figure represent failure lines, indicating potential failures at the trough points. The geological conditions of the K-NET Oiwake (HKD127) station are provided in Table 3 and Fig. 10.

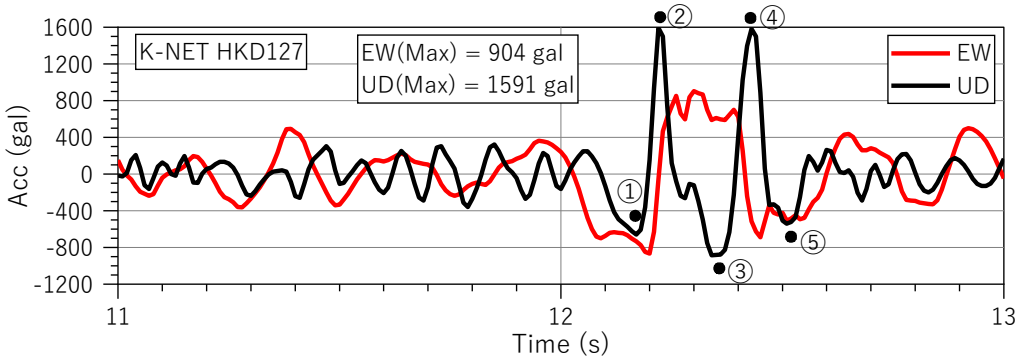

Fig. 8 Acceleration time history waveforms of UD and NS components (HKD127)

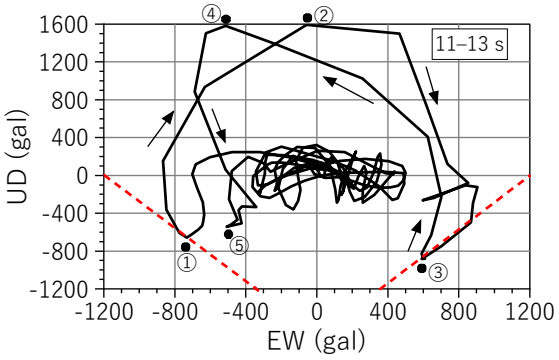

Fig. 9 Acceleration orbit of UD and EW components (HKD127)

Table 3 Underground structure at K-NET Oiwake

Depth (m)	Thickness (m)	V_s (m/s)	V_p (m/s)	ρ (g/cm^3)
1	1	130	480	1.47
2	1	130	480	1.52
3	1	160	1160	1.59
4	1	160	1160	1.64
5	1	160	1160	1.72
6	1	160	1160	1.71
7	1	160	1160	1.72
8	1	480	1760	1.73
9	1	480	1760	1.72
10	1	480	1760	1.80

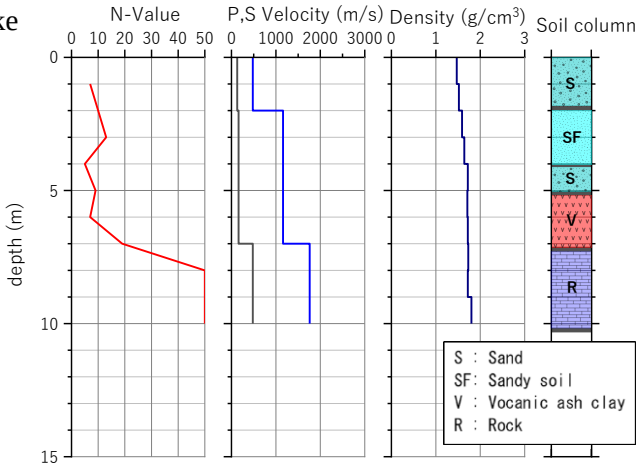

Fig. 10 Soil column diagram at K-NET Oiwake

3. ON THE VERTICAL MOTION CAUSED BY DILATANCY

In this section, we discuss the vertical acceleration and displacement generated by the dilatancy of the surface layer, based on constant-pressure cyclic direct box shear tests, microscopic studies, and elastoplastic theory. According to geotechnical engineering textbooks, materials with negative dilatancy, such as dry loose sand, exhibit volumetric compression under shearing. In contrast, materials with positive dilatancy, such as dense sand, undergo volumetric expansion.

3.1 Constant-pressure cyclic direct box shear tests (Displacement controlled)

The cyclic direct shear apparatus is equipped with servo motors for controlling both the normal and shear directions independently, allowing for precise control of displacement and stress. The test was conducted on medium-dense silica sand No. 3 (e_{max} = 0.963, e_{min} = 0.677, dry density ρ_d = 1.46 g/cm^3, and D_r = 51%). The specimen had a diameter of 6 cm and a height of 2 cm.

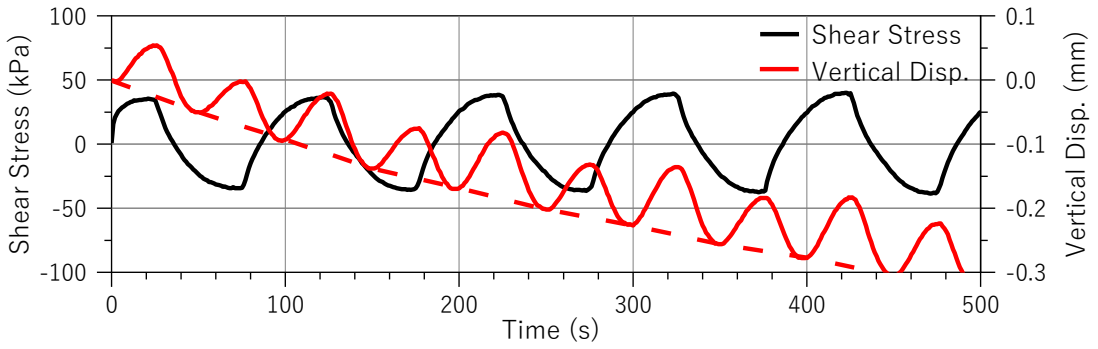

Fig. 11 Shear stress and vertical displacement time histories from the constant-pressure cyclic direct box shear test (medium-dense silica sand No.3)

Figure 11 illustrates the relationship between shear stress and vertical displacement from a constant-pressure cyclic direct box shear test, conducted under a confining pressure (vertical stress) of σ = 50 kPa. This involved 10 cycles of shear displacement with an amplitude of ±0.5 mm and a loading period of 100 s. For discussion purposes, the first five cycles are shown in Fig. 11. Although volumetric expansion (upward displacement) occurs at the peaks of positive and negative shear stresses, the residual settlement increases with the number of shearing cycles, indicating an accumulation of volumetric compression.

Figure 12(a) shows a gradually descending downward convex path of shear and vertical displacements over the ten cycles. The dotted red line in Fig. 11 connects the points where the shear displacement returns to zero. Nonlinear behavior is evident in the shear stress versus shear displacement relationship, as depicted in Fig. 12(b). By dividing the shear displacement by the specimen height (see Eq. (3) in Reference 11), the displacement can be converted to shear strain. For example, a shear displacement of ±0.5 mm corresponds to a shear strains of ±2.5%.

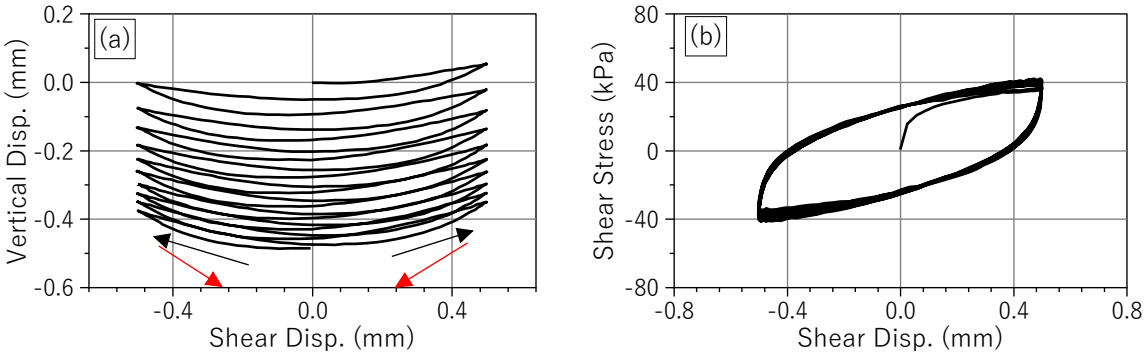

(a) Displacement path (b) Shear stress–shear displacement relationship

Fig. 12 Displacement path and Shear stress–shear displacement relationship

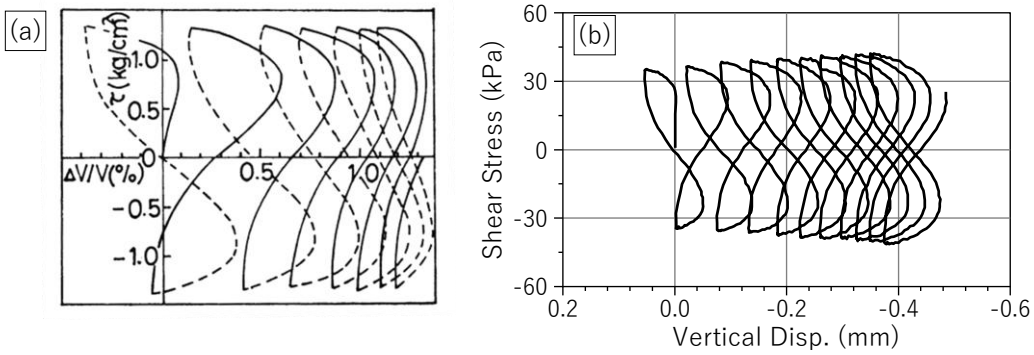

(a) Toyoura sand[12] (b) Silica sand No.3

Fig. 13 Shear stress–volumetric strain relationship

For comparison, Fig. 13(a) shows the relationship between shear stress and volumetric strain for dense Toyoura sand from a cyclic simple shear test by Yagi et al.[12]. Figure 13(b) presents the corresponding results for medium-dense silica sand No. 3 from the tests depicted in Fig. 11 and 12. Both figures exhibit similar volume change characteristics, indicating that residual volumetric compression occurs even in dense sand[12), 13)]. Similar behavior is observed in cyclic simple shear tests of a sand-gravel mixture with relative densities ranging from D_r = 20%–80% (Iwamoto et al.[13)]). It is also noteworthy that the gradual increase in shear stress amplitude in Fig. 13(b) results from increased density due to cyclic shear, whereas the test shown in Fig. 13(a) was conducted under stress-controlled conditions.

Figure 14 illustrates the impact of density on volumetric changes in loose, medium, and dense sand (with D_r = 30%, 51% and 90%, respectively). The tests were conducted under a confining pressure σ = 50 kPa and with a shear displacement amplitude of ±0.5 mm. The loose and medium-dense specimens were prepared by air pluviation, while the dense specimen was prepared using three layers of compaction. Similar to the experimental results of Iwamoto et al.[13], even in dense sand (Dr = 90%), some volume compression remains. The peak times of the vertical displacement in each cycle are consistent, and at the positive and negative peaks of the shear stress, volume expansion (upward displacement) occurs in the opposite direction to the residual displacement. The displacement amplitude is small in the first few

cycles of the loose sand, but thereafter there is little difference due to density. The vertical displacement amplitude in the final cycle (in mm) is also shown in the figure.

Figure 15 shows the relationship between shear and normal displacements for the first 1/4 cycle (from 0 to 25 s), which can be considered equivalent to a monotonic shear test. The figure indicates that loose sand undergoes volumetric compression, while medium and dense specimens exhibit volumetric expansion, consistent with classic soil mechanics theory. Even if the material shows volume expansion at this point, the volume compression remains when the shear stress returns to zero at the end of 1/2 cycle or 1 cycle.

In summary, two mechanisms appear to be associated with volumetric changes during the shear deformation of granular materials: (1) irreversible volume changes, or residual displacements, and (2) reversible volume changes, associated with vertical displacements during each cycle. The displacement generated by this reversible volume change is in the upward direction (volume expansion).

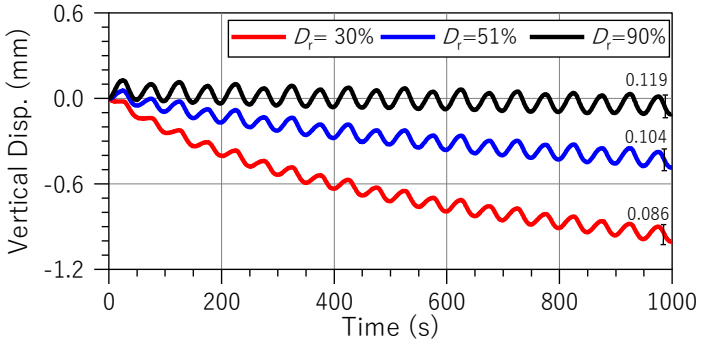

Fig. 14 Vertical displacement time histories of loose, medium and dense sand

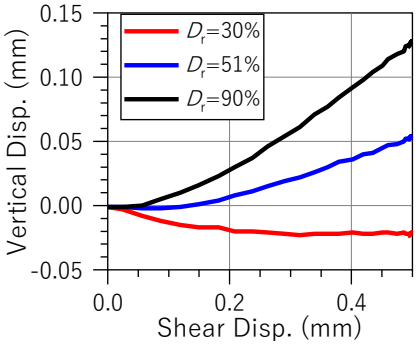

Fig. 15 Shear and vertical displacement path for the first 1/4 cycle

3.2 Microscopic consideration

Since dilatancy of soil is generated by the movement of soil particles due to shear stress, by conducting microscopic studies at the soil particle level, we will clarify the mechanism of vertical movement caused by dilatancy.

According to Murayama[2), 3)], the elastoplastic stress–strain relationship of sand can be associated with probability functions of the force angle β_i and the contact angle θ_i. The force angle β_i is defined as the angle between the interparticle force and the maximum mobilized plane ($(\tau/\sigma)_{max}$ plane) where the relative movement of the particles is most active. The contact angle θ_i is the angle between the slip slope when a particle i slides on the surface of an adjacent particle with respect to the $(\tau/\sigma)_{max}$ plane. In a direct box shear test, the $(\tau/\sigma)_{max}$ plane is the horizontal plane. The condition for initiating sliding on the $(\tau/\sigma)_{max}$ plane is expressed by the Eq. (1) in Reference 3), as follows.

$$\theta_i + \delta < \beta_i \tag{1}$$

Here, δ represents the average inter-particle friction angle. The right-hand side corresponds to the external force, and the left-hand side corresponds to the sliding resistance.

Under this condition, a reversible volume change occurs because the particle is deflected upward from the $(\tau/\sigma)_{max}$ plane by the contact angle θ_i . However, no residual strain is generated through cyclic shear. In other words, this elastic state is not truly elastic, satisfying Hooke's law[2), 3)]. The resulting volume expansion $-d\varepsilon_n$ (with compression considered positive) is expressed, by the Eq. (26) in Reference 3), as follows.

$$-d\varepsilon_n = \tan\theta_s \cdot d\gamma_\beta \tag{2}$$

Here, θ_s is the average value of θ_i, while γ_β represents the macroscopic shear strain on the $(\tau/\sigma)_{max}$ plane.

On the other hand, plastic deformation occurs when the stress ratio exceeds the elastic limit, leading to an irreversible residual strain. The elastic limit is the structural strength that resists the particle structure from decomposing into an irreversible state, and is called the potential barrier. In addition, the phenomenon in which sliding particles break down the potential barrier and push into the barrier's interior is called activation. When particles on the sliding slope are stopped by the potential barrier, particles return to their initial positions under the following condition (Eq. (6) in Reference 3)).

$$\beta_i + \delta < \theta_i \tag{3}$$

In the study conducted by Murayama[2), 3)], it was found that granular materials undergo both reversible and irreversible volume changes during shear deformation. While this model may not fully capture the dilatancy behavior during bidirectional cyclic shear, it serves as a theoretical framework for the sliding model. For bidirectional shearing, shearing in the opposite direction can be assumed to occur on a conjugate plane that satisfies Eq. (1). According to the sliding block theory framework, the condition for the block to ascend the slope at points ④ and ⑧ in Fig. 6(c) of Reference 14) is expressed by Eq. (1), whereas points ① and ⑤ correspond to Eq. (3). In other words, the portion between the trough and the subsequent crest in Fig. 11 can be associated with $d\gamma_\beta$ in Eq. (2).

In the "Bowl" model proposed by Fukutake and Matsuoka[4)], material behavior is characterized by the sum of reversible expansion and irreversible compression components. Additionally, Shamoto et al.[5)] suggest that reversible volumetric changes during shear are influenced by the current shear strain amplitude and direction, while irreversible volumetric changes are influenced by the shear history.

In Fig. 11 and 14, shear stress exceeding the elastic limit formed by the past stress history (from consolidation during the test) acts, and particles in both elastic and plastic states coexist. As the number of cycles increases, a new elastic limit is formed due to the transfer of interparticle forces from the activated particles (strain-hardening), and no particles in the plastic state are produced. Eventually, the plastic deformation will cease if the new elastic limit exceeds the applied shear stress.

In Fig. 14, it is evident that the residual displacement varies significantly with the density of the sand. On the other hand, the amplitude of the fluctuating vertical displacement does not change significantly. The double amplitude of the final cycle in Fig. 14 is 0.086 mm for loose sand, 0.104 mm for medium-dense sand, and 0.119 mm for dense sand. Since the residual displacements for loose and medium-dense sand have not yet converged, it can be inferred that the vibration amplitudes in each cycle are approximately the same across the three types of sand. According to Eq. (2), the average contact angle θ_s at the final stage for all three sand types should also be comparable, given that the shear strain $d\gamma_\beta$ in these tests is the same. By taking 0.104 mm as $-d\varepsilon_n$ for medium-dense sand and using the shear displacement as $d\gamma_\beta$, a rough estimate of $\tan\theta_s = 0.21$ (12°) can be obtained. This value is comparable to the $\tan\theta_s = 0.20$ (11°) estimated from a test on Toyoura sand (Fig. 3 in Reference 5)), where the final cyclic strain $\gamma = \pm 1.5\%$ and the reversible volumetric strain $\varepsilon_{vc,re} = -0.3\%$ (volume expansion).

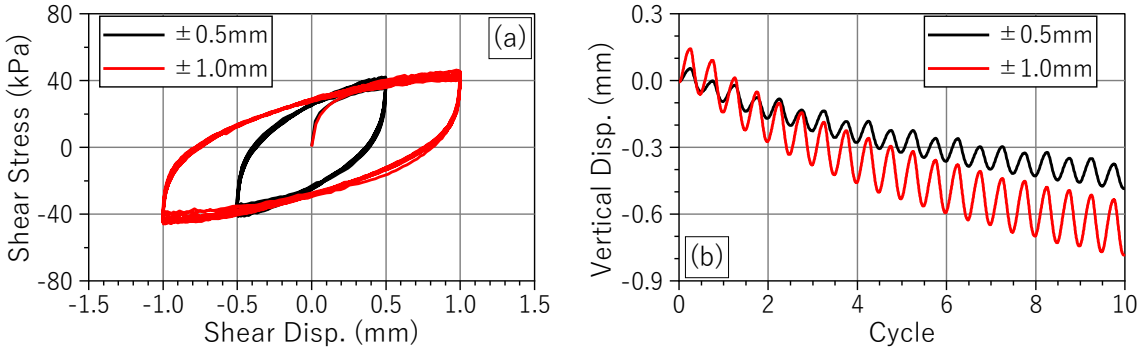

(a) Shear stress–shear displacement (b) Vertical displacement time histories

Fig. 16 Effect of shear displacement amplitude (σ = 50 kPa)

Figure 16 illustrates the effect of shear displacement amplitude (±0.5 mm and ±1.0 mm) on direct box shear tests of medium-dense sand (silica sand No. 3). It is important to note that the shearing period for the ±1.0 mm test was extended to 200 s to match the shearing rate between the two tests. As shown in Fig. 16(a), the shear stress reaches a plateau at nearly the same value regardless of whether the shear displacement is doubled. In contrast, the vertical displacement amplitude increases proportionally with the shear displacement amplitude, with 0.104 mm for the ±0.5 mm test and 0.225 mm for the ±1.0 mm test.

The confining pressure is a crucial factor influencing the strength and deformation characteristics of soil, as demonstrated by the test results for medium-dense silica sand No. 3 shown in Fig. 17. The figure presents four curves obtained from tests with confining pressures of 25, 50, 100, and 200 kPa, using a shear amplitude of ±0.5 mm. As depicted in Fig. 17(a), both the shear modulus and shear strength vary significantly with confining pressure. However, the vertical displacement amplitude remains unchanged with different confining pressures, as shown in Fig. 17(b). Additionally, the stress ratio (τ/σ) versus shear displacement relationship in Fig. 17(c) is consistent across the different confining pressures.

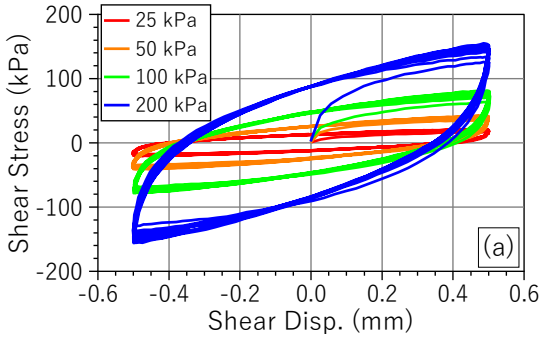

(a) Shear stress–shear displacement relationships

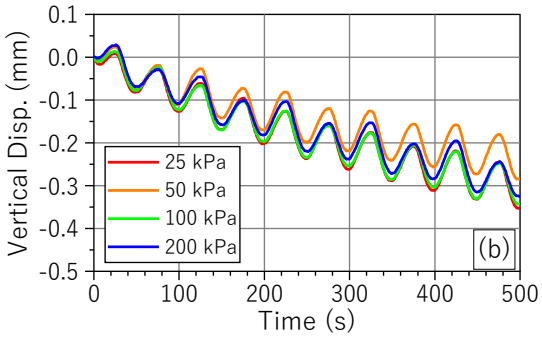

(b) Vertical displacement time histories

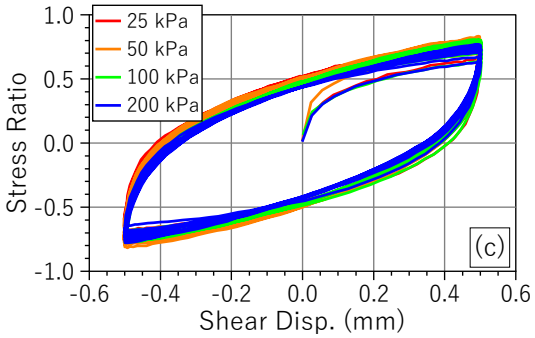

(c) Shear stress ratio–shear displacement relationships

Fig. 17 Medium-dense silica sand No. 3 with confining pressures of 25, 50, 100, and 200 kPa

This indicates that the parameter θ_s in Eq. (2) is influenced by the sedimentary environment but is less affected by confining pressure (depth of the ground). Therefore, it can be concluded that variations in vertical displacement correspond to reversible volume changes, which can be geometrically[15] determined according to Murayama's works[2), 3)].

Based on the results shown in Fig. 14, it can be concluded that the vertical motion induced by soil dilatancy is not significantly affected by soil density or confining pressure. Instead, it increases with the shear strain amplitude. Consequently, this vertical motion becomes more pronounced when shear strain is amplified in low-velocity soil layers near the ground surface.

3.3 Consideration based on elastoplastic theory

In the strong earthquake estimation, the ground is treated as a continuum that transmits seismic waves. In this section, we investigate the relationship between dilatancy and vertical motion based on elastoplastic theory, which treats ground as a continuum.

3.3.1 Positive and negative dilatancies

Sekiguchi[16] used the Cam Clay model[15] to describe the accumulation of plastic volumetric compression observed in normally consolidated and lightly overconsolidated clays under constant-pressure shearing tests, referring to it as negative dilatancy, while the plastic volumetric expansion observed in heavily overconsolidated clays was called positive dilatancy. These plastic volume changes are residual displacements that accumulate in one direction in Fig. 11 and 14. Since the plastic strain increment $d\varepsilon^{p}$ does not produce a stress increment within the framework of elastoplastic theory, the residual displacement has no effect on the generation of vertical acceleration in dynamic problems involving inertial forces. In this paper, we term the accumulation of volumetric plastic compression due to repeated shearing as negative dilatancy to distinguish it from the cumulative volumetric plastic expansion associated with positive dilatancy (see Fig. 14 in Reference 1) and Fig. 14 in Reference 17)).

The contact angle θ_s in Eq. (2) is the dilatancy angle on the Mohr's circle of strain increment (Eq. (8.13) in Reference 15), Eq. (2a) and (26b) in Reference 14), etc., see Appendix 2). The left-hand side of Eq. (1) indicates that strength (sliding resistance) is the sum of frictional and dilatancy resistances[15].

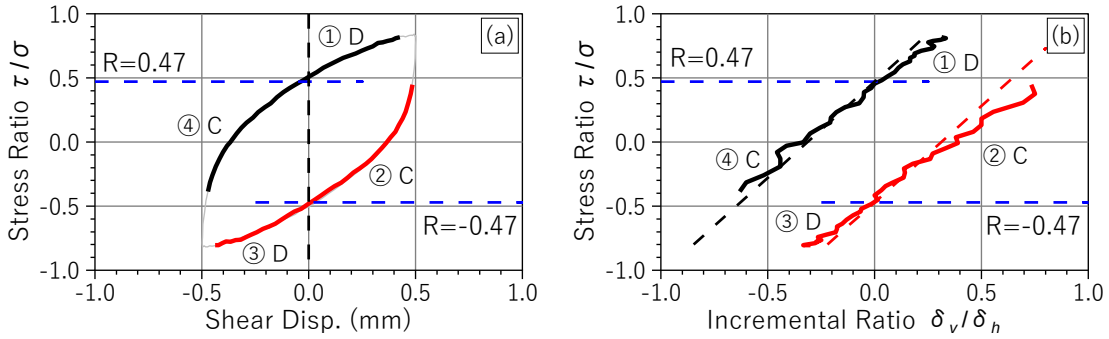

(a) Shear stress ratio and shear displacement relationship (b) Stress–dilatancy relationship

Fig. 18 Stress–dilatancy relationship of medium-dense silica sand No.3 (σ = 50 kPa)

Figure 18(a) illustrates the relationship between the shear stress ratio (τ/σ) and shear displacement δ_h from the final cycle of the test on medium-dense silica sand No. 3. Figure 18(b) is stress–dilatancy relationship, which is the relationship between (τ/σ) and the incremental displacement ratio (δ_v/δ_h). Here, the total strain increment is approximately considered as the plastic strain increment. Note that the portion of the graph immediately following the unloading point is omitted due to significant numerical fluctuations that occur when dividing the vertical displacement increment by a very small denominator. As shown in Fig. 18(b), when the stress ratio R is ±0.47, the vertical displacement, or dilatancy, becomes zero. This stress ratio is indicated by the dashed blue line in Fig. 18 for reference. When the magnitude of the stress ratio exceeds 0.47 (denoted by zones ①D and ③D), volumetric expansion occurs. In contrast, for zones ②C and ④C, which involve the unloading stage, volumetric compression is observed. Figure 18(b) also shows that a line of constant stress ratio intersects two incremental displacement ratio points. This type of material can be modeled by assuming two plastic potential functions that intersect at the same stress point[14]. The stress–dilatancy function is expressed by the following equation (Eq. (43) in Reference 14)). This equation can be regarded as an extension of Eq. (38) in reference 3) to bidirectional cyclic shearing.

$$\frac{\tau_{at}}{\sigma_a} = \pm\tan\phi_\mu + s\left(-\frac{dV_d}{d\gamma_{at}{}^p}\right) \tag{4}$$

Using the same parameters ($\tan\phi_\mu = 0.47$, $s = 1.5$, and the failure line R = ±0.8) as in the study on Toyoura sand by Pradhan and Tatsuoka[14], the dotted black and red lines can be plotted in Fig. 18(b). These synthetic lines correspond relatively well with the test results.

The tendency for negative dilatancy (a significant decrease in effective stress) accompanying the reversal of shear direction is a crucial factor in elastoplastic undrained analysis[16]. This behavior is reflected in the largest volume compression rate ($\delta_v/\delta_h \fallingdotseq \pm 0.8$) immediately after unloading in regions ②C and ④C of Fig. 18(b). This volumetric compression is proportional to the stress ratio at which unloading occurs[14]. At the peaks of the shear displacement in Fig. 12(a), the gradient of the volumetric compression during unloading (red arrow) is steeper than the gradient of the volumetric expansion during loading (black arrow). Therefore, the displacement path follows a hysteresis loop. When the generation of plastic particles diminishes[2), 3)], the displacement path will return to the same location in each cycle, resulting in a closed hysteresis loop. In other words, the vertical displacement amplitude in the expansion region ①D is equal to that in the compression region ②C. This phenomenon suggests that the volumetric work increment is absorbed by the friction component[15].

The contact angle θ_s, force angle β_i, and the average inter-particle friction angle δ mentioned in Reference 3) are correspond to the dilatancy angle ψ, effective friction angle ϕ_m', and the stress ratio μ (ϕ_{cs}') at critical state ($\delta_v/\delta_h = 0$) in Reference 15), respectively.

The shear stress reversals in Fig. 18(b) can be distinguished based on whether they are coaxial where the principal stress axes and the principal incremental axes of plastic strain coincide, or non-coaxial (see Fig. 7 and 9 in Reference 14)). By introducing a scalar variable c ($-1 \leq c \leq 1$) that represents the degree of non-coaxiality in the stress–dilatancy relationship (see Eq. (12) and Fig. 4 in Reference 18)), it is possible to simulate the experimental results in the general stress space.

In this study, the direct box shear test was regarded as "equivalent to a simple shear test or a plane strain test in which the shear plane coincides with the sedimentary (horizontal) direction[19)]". This assumption is deemed valid for the qualitative evaluation of dilatancy characteristics, as illustrated in Figs. 13 and 18. However, the original objective of the direct box shear test is to "determine the strength parameters required for stability analysis of ground using the limit equilibrium method as per the Coulomb failure criterion[19)]". To quantitatively assess these parameters, it is essential to compare and verify the results with those from simple shear or plane strain tests.

Additionally, because it was not possible to obtain samples from the observation points for testing in this study, direct box shear tests were conducted using silica sand No. 3 instead. The comparison of these results with the test results for Toyoura sand is presented in Figs. 13 and 18. It is considered that the test results for silica sand No. 3 qualitatively represent the dilatancy characteristics of typical sandy soils.

3.3.2 Response analysis based on classical elastoplastic theory (see Appendix 2)

We will attempt to represent the phenomena shown in Figs. 6 and 8 by using response analyses based on the classical elastoplastic theory[15), 20)–22)], which forms the backbone of the recent "cyclic model" (see Appendix 2).

Figure 19 presents the time history of horizontal acceleration, vertical acceleration, and vertical displacement at the ground surface when a sinusoidal horizontal motion (5 Hz, amplitude = 100 gal) is applied to a 10 m-thick ground layer. The residual settlement of approximately 5 mm is attributed to volumetric compression. During each yielding point in the cycle, volumetric expansion due to elastic strain increment $d\varepsilon^E$ occurs, resulting in downward acceleration and upward displacement at the positive and negative peaks of the horizontal acceleration, respectively. In other words, the direction of residual displacement opposes the displacement caused by vertical motion. Similar results can also be observed in the response analyses of dry ground using the Densification model [23)] (this model is developed for liquefaction analysis).

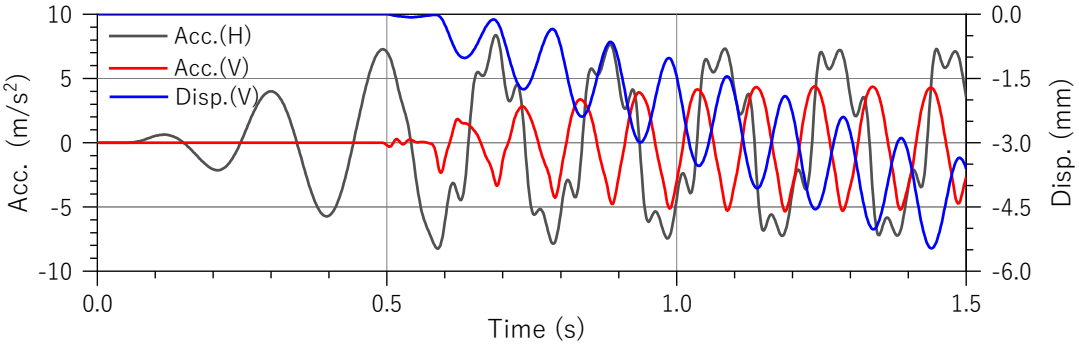

Fig. 19 Horizontal and vertical acceleration and vertical displacement time history waveforms

Figure 20 is derived from the data within the first 1 s of Fig. 19. It shows the stress path at the middle of the surface layer (element 5), with circular markers indicating the initial stress points. When the stress point reaches the failure line, it moves downward along the failure line toward the origin of the stress space, as illustrated by the red arrow.

Figure 21 depicts the relationship between shear strain γ and vertical strain ε_z, which is equal to volumetric strain ε_v. Similar to Fig. 12(a), the path is downwardly convex, gradually shifting downward throughout the test. In other words, residual vertical strain accumulates with the cyclic shear history.

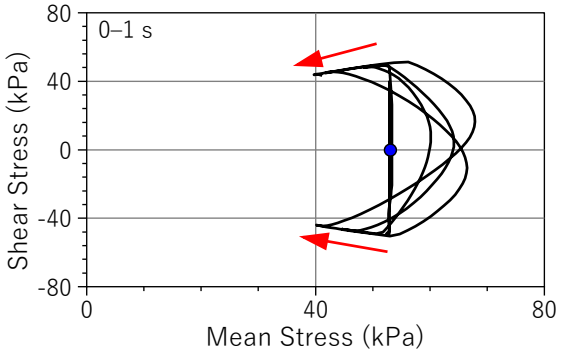

Fig. 20 Stress path

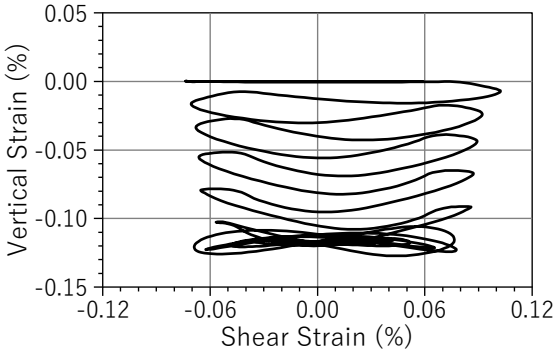

Fig. 21 Strain path

3.4 Discussion

Under consolidated undrained shear (CU Test), such as liquefaction and cyclic mobility phenomena, volumetric changes, vertical displacement and residual settlement, are restricted due to the incompressibility of water. Therefore, no vertical motion is generated. The volume change that would have occurred under drainage conditions is converted into effective stress via pore water pressure. In contrast, the phenomenon depicted in Figs. 6, 7, 8, and 9 is consolidated drained shear (CD Test). Although residual settlement associated with plastic deformation does not contribute to stress increments, vertical motion occurs, and a pronounced elastoplastic response occurs due to the coupling with horizontal motion. Which phenomenon occurs depends on differences in the moisture content and the drainage characteristics of the soil material.

The ground structure of the KiK-net Oiwake (IBUH01) station is shown in Table 2. The shear wave velocities *Vs* = 130 and 250 m/s for the silt layers until GL−4 m and ranging GL−4 m to GL−12 m, respectively. They are underlain by an engineering bedrock with *Vs* = 450 m/s. Since the groundwater level is not described in the Kik-net database, it was assumed based on the P-wave velocity that the groundwater level is assumed to be below GL−4m. While no soil mechanics tests were performed, it can be inferred that significant shear strain occurred in the top ground layer which has a low velocity.

The troughs shown in Fig. 6 (①, ③, ⑤, ⑦) are believed to be volumetric expansions[2)–5)] induced by this cyclic shear strain.

The ground structure of the K-NET Oiwake (HKD127) station is shown in Table 3 and Fig. 10. The shear wave velocities *Vs* = 130 m/s for a sand layer down to GL−2 m and 160 m/s for a mixed layer of sand, sandy soil and volcanic clay ranging GL−2 m to GL−7 m. They are underlain by an engineering bedrock with *Vs* = 480 m/s. Since the K-NET Oiwake (HKD127) station is only 100 m away from the IBUH01 station, the engineering bedrock is assumed to be the same. While no soil mechanics tests were performed, it is believed that the downward accelerations (indicated by the troughs ①, ③, ⑤ in Fig. 8) are due to the shear induced reversible volumetric expansion[2)–5)] in the top two layers.

This phenomenon is the generation of P waves from S waves due to the elastoplastic response of the surface ground. In Fig. 6, the downward accelerations approaching −1 G (e.g., −747 gal at ③ and −699 gal at ⑦) are generated by the positive NS component, which is thought to have released the initial stress and resulted in a strong elastoplastic response under low confining pressure. This interpretation is supported by the collapse of the NS2 component peaks at points corresponding to ③ and ⑦ and being wide trapezoidal shape. Additionally, the vertical motion plot reveals that the widths of the troughs at points ①, ③, ⑤, and ⑦ are greater than those of the crests at points ②, ④, ⑥, and ⑧. As confining pressure increases when vertical acceleration rises from the troughs to the crests, the ground stiffness also increases. This results in a stiffer response with narrower pulse widths and larger amplitude vertical motions. The maximum value of the UD2 component (1060 gal), shown in Table 1, is attributed to the upward acceleration at point ⑥.

In Fig. 8, a similar phenomenon is observed at point ③, where the downward acceleration close to −1 G (−884 gal) is generated by the positive EW component, which is thought to have released the initial stress and resulted in a strong elastoplastic response under low confining pressure. This interpretation is supported by the plateau shape of the EW waveform on the positive side corresponding to this point. Additionally, it is evident that the widths of the troughs at points ① and ③ are wider compared to the crests at points ② and ④. As confining pressure increases with vertical acceleration moving from the troughs to the crests, the ground stiffness also increases, resulting in a stiffer response with narrower pulse widths and larger amplitude vertical motions. The maximum value of the UD component (1591 gal), shown in Table 1, is attributed to the upward acceleration at point ②.

It should be noted that the surface soil of the KiK-net Ichinoseki-W (IWTH25) station, modeled as extremely overcosolidated clay by Asaoka et al.[17)], is completely different from those of the two stations considered in this study. The ground at Ichinoseki-W is covered by a stiff layer with *Vs* = 430 m/s and *Vp* = 850 m/s down to GL−6 m, and is underlain by an even stiffer layer with *Vs* = 530 m/s and *Vp* = 1770 m/s extending down to GL−34 m. The ground classification of Ichinoseki-W is clearly different from that of the two stations in this study. The top layer is very stiff and can be considered a rock outcrop layer.

3.5 Comparison between constant-pressure and constant-volume direct box shear tests

To illustrate the importance of soil mechanics testing in determining site characteristics (specifically ground amplification characteristics) during strong ground motion, Fig. 22 presents a comparison between constant-pressure direct box shear tests and constant-volume direct box shear tests on medium-dense silica sand No. 3. Figures 22(a) and 22(b) show the stress path and shear stress–displacement relationships, respectively. Both tests were conducted with a shear displacement amplitude of ±0.5 mm (equivalent to a shear strain of ±2.5%) and similar initial vertical stress.

The induced shear stress in the surface layer is related to the horizontal acceleration, as indicated by Eq. (5) (modified from Eq. (4) of Reference 24)). Assuming that the direct box shear test specimen represents a soil element located 3.5 meters below the ground surface, the overburden pressure at this depth is 50 kPa ($\sigma = \rho_d g z = 50$ kPa). Therefore, a normal pressure of 50 kPa is used for the constant-pressure direct box shear test. Under shearing with the specified displacement amplitude (±0.5 mm), the maximum shear stress of ±40 kPa is observed, which corresponds to a horizontal acceleration of ±0.8 G at the ground surface. It should be noted that the stress ratio in this test corresponds to the stress ratio R = ±0.8

as shown in Fig. 18. In other words, the shear strength of the surface layer represents the maximum horizontal acceleration at the ground surface.

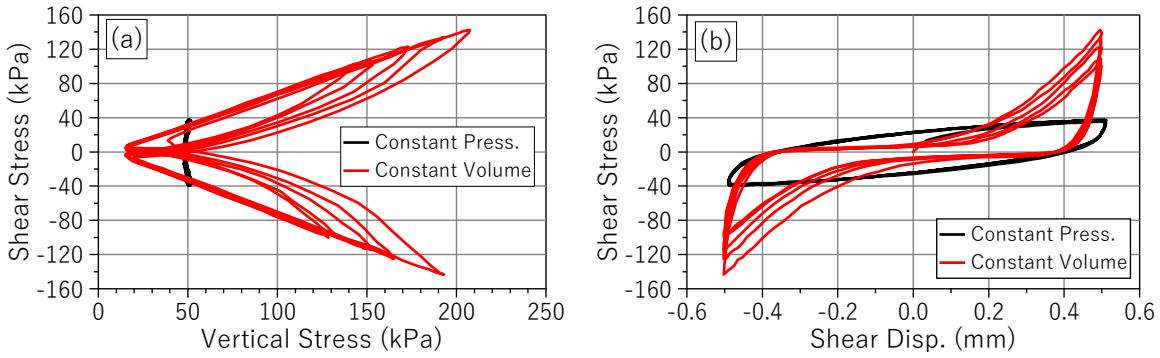

(a) Stress path (b) Shear stress–displacement relationships

Fig. 22 Comparison between constant-pressure and constant-volume direct shear on medium-dense silica sand No.3

$$\frac{Acc_{(surface)}}{g} = \frac{\tau(z)}{\sigma(=\rho g z)} \tag{5}$$

If we replace $\tau(z)$ on the right-hand side with the fluctuating vertical stress $\sigma_d(z)$, this equation also applies to vertical motion. The vertical stress due to gravitational acceleration (g = 1 G) is $\sigma_d(z)$ = 50 kPa (constant). This equation is applicable up to the corner frequency[24] $f_c = c/(2\pi z)$, where c is the wave propagation velocity.

In the constant-volume direct box shear test, the shear stress varies significantly ($\tau(z)$ = ±140 kPa) due to fluctuations in effective vertical stress (σ' = 15 kPa to 205 kPa). Although the specimen is dry, its stress state is comparable to the effective stress (50 kPa) of a saturated ground at a depth of z = 5.6 m, with a saturated density ρ_{sat} = 1.91 g/cm^3 and an effective unit weight γ' = 8.90 kN/m^3. Dividing $\tau(z)$ = ±140 kPa by the total stress σ_{sat} (= $\rho_{sat}\, gz$ = 105 kPa) gives a horizontal acceleration of ±1.33 G at the ground surface. However, under constant-volume shear (undrained conditions), no vertical acceleration occurs because the total stress ρ_{sat} is constant.

On the other hand, in dynamic problems involving inertial forces, vertical acceleration due to dilatancy becomes significant as the shear strain increases, under drained conditions (dry state). In this case, the stress path is qualitatively similar to that observed in the constant-volume direct box shear test. Starting from an initial stress condition of 50 kPa, when the ground moves upward (indicating volumetric expansion and negative acceleration), the stress point descends towards the origin of the stress space, leading to a reduction in both vertical stress and shear stress. Conversely, when the ground moves downward (indicating volumetric compression and positive acceleration), both vertical stress and shear stress increase along the failure line. Since the ground stiffness is influenced by the confining pressure (see Eqs. (A1) and (A3) in the appendix), and the failure line is defined by a constant stress ratio, the vertical acceleration is asymmetric in the upward and downward directions[25]. The increase in shear stiffness due to the rise in confining pressure is illustrated by the bending backward curves in Fig. 22(b).

Based on the settlement during consolidation for the constant-pressure direct box shear tests (Fig. 17), the settlement increases from 0.020 mm to 0.111 mm when the stress increased from 50 kPa to 200 kPa. The settlement increment is 0.091 mm for the stress increment $\Delta\sigma$ = 150 kPa. On the other hand, the amplitude of vertical displacement due to dilatancy is 0.104 mm as determined from the final cycle of the curve in Fig. 14 (σ = 50 kPa, shear displacement amplitude = ±0.5 mm).

These phenomena are caused by shear failure[1] (yielding) of soil under a compressive stress state, and during the strong ground motion that causes these phenomena, the maximum horizontal and vertical

accelerations at the ground surface are affected by the shear strength and dilatancy characteristics of the surface layer. Since the stress ratio of the failure line is generally $|R| < 1$, it is assumed that horizontal accelerations at the ground surface exceeding ±1 G are affected by coupling with vertical motions under drained conditions or by fluctuations in effective vertical stress under undrained conditions (cyclic mobility phenomenon).

The significance of dilatancy in the surface ground under undrained conditions is well recognized among researchers. However, similar phenomena in dry soils have received relatively little attention. This is likely because the effects in dry soils are less evident compared to the clear traces observed in cases of liquefaction.

4. SUMMARY

During the 2018 Hokkaido Eastern Iburi Earthquake, downward accelerations (volume expansion) caused by the dilatancy of the surface ground were observed at the KiK-net Oiwake (IBUH01) and K-NET Oiwake (HKD127) stations. The generated vertical accelerations were strongly coupled with horizontal accelerations. This phenomenon can be attributed to the reversible volumetric changes inherent in granular materials. These volumetric changes are relatively unaffected by ground density or confining pressure but increase with the amplitude of shear strain. As a result, vertical motions due to dilatancy are more pronounced in low-velocity surface layers.

Downward accelerations close to −1G were recorded at the KiK-net Oiwake station (−747 gal) and at the K-NET Oiwake station (−884 gal). These downward vertical motions indicate a strong elastoplastic response under low confining pressure. The frequency of the vertical motion is twice that of the horizontal motion, a phenomenon also noted in the strong motion record at the KiK-net Mashiki (KMMH16) station during the 2016 Kumamoto Earthquake (M6.5 foreshock on April 14th, see Appendix 3). This phenomenon corresponds to the fluctuation of pore water pressure at twice the frequency of the loading cycle observed in liquefaction strength tests.

5. AFTERWORD AND CHALLENGES

Asaoka et al.[17] described the series of commotions caused by the 2008 Iwate-Miyagi Nairiku Earthquake, which recorded large accelerations of over 4 G at the KiK-net Ichinoseki-W (IWTH25) station, as being "the mountains have brought forth a mouse". In the field of geotechnical engineering, crucial insights [for example 26), 27)] for understanding the strong elastoplastic responses of surface ground during earthquakes have been developed. These include concepts such as dilatancy, anisotropy, non-coaxiality, strain softening (stress drop and residual strength), shear band formation and movement of pore water into the shear band, unsaturation, partial drainage, and the strength and deformation characteristics of soil materials. Additionally, numerous (visco) elastoplastic constitutive models[28] have been proposed based on these insights. Understanding various phenomena observed in the ground during strong earthquakes requires a solid grasp of soil mechanics[17].

Liquefaction and cyclic mobility phenomena are consolidated undrained shear (CU Test). In other words, these are constant-volume shear in which the volume change of soil skeleton (vertical acceleration) caused by shear (horizontal acceleration) is constrained by incompressible pore water. In contrast, the phenomenon described in this report is consolidated drained shear (CD Test), which produce a strong elastoplastic response through the interaction of generated vertical and horizontal motions. The changes in the radius and movement of the Mohr's (effective) stress circles[29] are more pronounced in this case compared to liquefaction phenomena. Both types of behavior arise from differences in soil water content and drainage characteristics.

Many studies have explored the applicability of elastoplastic constitutive models to undrained shear conditions. However, a significant challenge remains in determining whether these models can quantitatively simulate vertical motion caused by dilatancy and its interaction with horizontal motion

under dry conditions. Additionally, while site characteristics during minor earthquakes, which involve only horizontal motion, have been studied, further research is needed to understand how these characteristics evolve during strong earthquakes where horizontal and vertical motions are coupled. Locations with large acceleration records, such as those discussed in this study, offer valuable insights into these phenomena. It is essential to "at least" confirm the groundwater level by borehole survey at these sites and to carry out a series of physical and mechanical tests based on the so-called "Red Book[30)]" to examine the strength and dilatancy characteristics of the surface ground.

As highlighted in Section 3.5, geotechnical tests are crucial for understanding site characteristics, such as ground amplification during strong ground motions. Anisotropy[31)] also plays a significant role in these characteristics. Specifically, regarding strength characteristics, Tatsuoka and Paku[32)] demonstrated that the internal friction angle ϕ can differ by 7° under the same plane strain conditions, underscoring the importance of strength anisotropy. This anisotropy becomes even more pronounced in the general stress space.

A thorough study is essential, whether under undrained or dry conditions, based on the fundamental characteristics of soil materials that underpin elastoplastic constitutive models. It is crucial to investigate these characteristics to understand the strong elastoplastic response of surface ground during strong earthquakes. It is like "Putting the cart before the horse" to discuss deformation characteristics without examining strength characteristics and anisotropy. Hence, incorporating more in-depth soil mechanics knowledge is necessary.

ACKNOWLEDGMENT

In this study, we utilized strong motion records and ground survey data from the K-NET and KiK-net networks, provided by the National Research Institute for Earth Science and Disaster Resilience. We also extend our gratitude to Emeritus Professor Yoshio Tobita from Tohoku Gakuin University for his invaluable insights into elastoplastic constitutive models of soils and microscopic studies, which significantly contributed to the preparation of this paper.

APPENDIX 1.

Although SHAKE[33)] is proposed for simulating the propagation of SH waves in vertical direction, it can also be used for the propagation of P waves. In this case, the boundary conditions, stresses, strains, and other factors are all the same as those in Terzaghi's consolidation theory (K_0 consolidation), which is one of the most famous theories in geomechanics. Consolidation phenomena is the process in which the compressive deformation of soil (sinking of the soil skeleton in water) is slowed by the resistance of pore water. An increase in consolidation load corresponds to the upward acceleration of vertical movement. For this purpose, the vertical strain ε_Z is used instead of shear strain γ, (since no lateral strains are assumed, $\varepsilon_X = \varepsilon_Y$ = zero, the volume strain ε_V is also equal to the vertical strain ε_Z). Similarly, the vertical stress σ_Z is used instead of shear stress τ whereas Vp and constraint modulus $K+(4/3)G$ are used instead of Vs and G, respectively.

That is, the volumetric compressibility coefficient m_v in Terzaghi's consolidation theory is given by Eq. (A1).

$$m_v = \frac{1}{K + \frac{4}{3}G} = \frac{1}{\rho {V_p}^2} \tag{A1}$$

This equation is extremely important for verifying FEM programs based on the Biot's formula, including the analysis of settlement due to liquefaction. It should be noted that m_v cannot be expressed by any formula other than the one above.

The elucidation of the strong elastoplastic response that couples horizontal and vertical motions, as

mentioned in the main text, requires a thorough understanding of the hysteresis characteristics of vertical motion (the relationship between mean stress σ_m and volumetric strain ε_V). It is well known that the hysteresis characteristics in consolidation test[30] are evaluated by the compression index *Cc* and swelling index Cs.

APPENDIX 2.

We examine how the direction of vertical acceleration and displacement generated by soil dilatancy, as well as particle orbits, can be expressed within the scope of flow rule used in classical elastoplastic theory[15), 20)–22)], which forms the backbone of the "cyclic model." The following Drucker–Prager criterion is used as the yielding surface and for the plastic potential surface, the non-associated flow rule[15), 20)] is adopted in which the internal friction angle ϕ in the same equation is replaced with the dilatancy angle ψ.

$$f = \alpha\sigma_m + \sqrt{J_2} - k = 0$$
$$\alpha = \frac{2\sqrt{3}\sin\phi}{3-\sin\phi} \qquad k = \frac{2\sqrt{3}c\cos\phi}{3-\sin\phi} \tag{A2}$$

Here, σ_m is the mean stress, J_2 is the second invariant of deviatoric stress, c is the cohesion. For the plastic potential surface, k is determined by constraining the surface to pass through the current stress point. This model follows the associated flow rule when $\psi = \phi$, and the plastic potential surface becomes Mises-type when $\psi = 0$. Additionally, positive dilatancy characteristics are represented when $\psi > 0$, and negative dilatancy characteristics are represented when $\psi < 0$. Reference 21) was used as the Fortran subroutine for the constitutive law. The verification of the analytical method was carried out by comparing the results with the analyses using the general-purpose structural analysis program MSC·NASTRAN[23)].

As mentioned with respect to Fig. 19, the thickness of surface soil layer is assumed to be 10 m similar to that shown in Chapter 5 of Reference 1), input seismic motion (horizontal motion of 5 Hz, Max = 100 gal), material properties (ρ = 1.8 t/m^3, *Vs* = 200 m/s, Poisson's ratio = 0.26), strength properties (c = 15 kPa, ϕ = 30°, hardening coefficient K_p = 0), numerical integration method (Newmark's β method, dt = 0.002 s), and nonlinear convergence calculation method (initial stress method) were used. The dilatancy angle ψ was set to −15°, and Rayleigh damping with α = 0.6021 and β = 0.0009616 was applied. This damping was set to have a damping coefficient of 3% at 2 Hz and 3.5% at 10 Hz which is the frequency of vertical motion generated by dilatancy. The damping is an important consideration for this analysis.

In classical elastoplastic theory[20)–22)] including the previous model[1)], the elastic stiffness (G, K) is assumed to be constant, but in this analysis, the dependency of G on confining pressure (mean stress σ_m) is considered as follows:

$$G = G_0\left(\frac{\sigma_m}{\sigma_{m0}}\right)^{1/2} \tag{A3}$$

Here, σ_{m0} is the initial mean stress, and G_0 represents the shear stiffness at σ_{m0}. The volumetric modulus K is also expressed by the same equation using K_0 and σ_{m0}. In other words, it assumes surficial ground with *Vs* = 112 m/s–235 m/s (*Vs* = 200 m/s at the center which is located at GL−5m).

Figure 19 shows the horizontal acceleration, vertical acceleration, and vertical displacement time histories at the ground surface. Figure A1 shows the acceleration orbit of horizontal and vertical motion at the ground surface. Additionally, Figure A2 shows the orbit of the NS component and UD component at K-NET Tsukidate (MYG004), which recorded seismic intensity 7 during the 2011 off the Pacific Coast of Tohoku Earthquake[36)]. By evaluating the dependency of the elastic stiffness on confining

pressure, the downward acceleration has plateaued and the downward pulse width has widened. The peculiar inverted concave-shaped acceleration orbit observed in K-NET Tsukidate is expressed, albeit qualitatively.

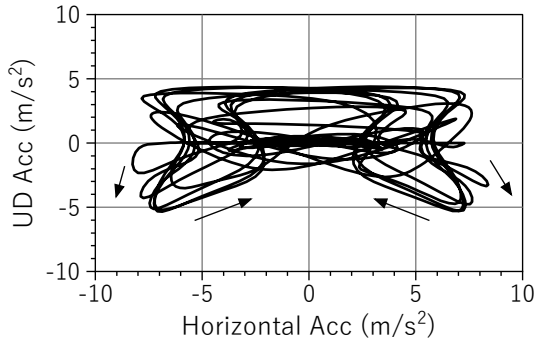

Fig. A1 Acceleration orbit of UD and NS components

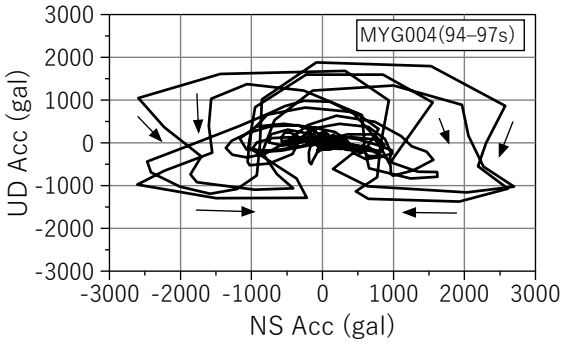

Fig. A2 Acceleration orbit of UD and NS components (K-NET Tukidate)

APPENDIX 3.

In the Kumamoto Earthquakes that occurred on April 14, 2016 at 21:26 (Fore shock M6.5) and on April 16, 2016 at 1:25 (Main shock M7.3), a maximum seismic intensity of 7 was observed at KiK-Net Mashiki (KMMH16). The peak acceleration at the ground surface when combined from all three components was 1580 gal for the fore shock and 1362 gal for the main shock. The maximum accelerations at the borehole (GL−252 m) and at the ground surface and amplification factors for both earthquake records are summarized in Table A1. Despite the Fore shock (M6.5) having a smaller earthquake magnitude compared to the mainshock (M7.3), the observed maximum accelerations were actually larger. It shall be noted that the amplification factor for vertical motion being as high as 11.0 times. The ground data for KiK-Net Mashiki (KMMH16) is shown in Table A2.

Figure A3 shows the vertical acceleration time history waveforms (from 16 to 20 s) at the borehole (UD1) and at the ground surface (UD2) during the fore-shock (M6.5). The black slant lines are connecting UD1 and UD2 components at around the same phase. The average propagation velocity, V=1480 m/s. It can be observed that the UD2 component resembles the UD1 component before the arrival of strong horizontal motion at around 18.5 s. After 18.5 s, the similarity between UD1 and UD2 deminishes. The red dashed line and red solid line are drawn by matching between the troughs in UD1 and UD2 component at the locations marked by ●. It seems that the high-frequency component disappears from the measurement at the ground surface (UD2). Among these, it seems that the magnitude of UD2 is significantly larger than the incident wave from UD1 at positions ③ and ④. The maximum acceleration of UD2 at the crest marked by red circle between ③ and ④ is 1399 gal. This large scaling suggests that UD2 may be affected by some additional factors beyond the normal amplification phenomenon during wave propagation.

Figure A4 shows the vertical acceleration UD2 and the larger horizontal acceleration EW2 (from 18 to 21 s) at the ground surface. The ● symbols at ①–④ are at the same positions as in Fig. A3 and the red circle also represents the maximum acceleration of 1399 gal. The downward vertical acceleration of ①–④ occur slightly later than the crests and troughs of the EW2 component. The mark ① and ③ correspond to the troughs of the EW2 component, while the mark ② and ④ correspond to the crests. The frequency of vertical motions is twice that of horizontal motions. Figure A5 shows the acceleration orbit of UD2 and EW2 (from 18.5 to 20.5 s). The ● symbols at ③ and ④ and the red circle represent the same instance as in Figs. A3 and A4. The failure line is marked in red dashed line when considering the figure as a stress path.

Table A1 Maximum acceleration and amplification factor

	Component	(gal)	Component	(gal)	Amplification factor
Fore	NS2	760	NS1	237	3.2
shock	EW2	925	EW1	178	5.2
April 14	UD2	1399	UD1	127	11.0
Main	NS2	653	NS1	159	4.1
shock	EW2	1157	EW1	243	4.8
April 16	UD2	873	UD1	196	4.5

Table A2 Ground data for KiK-Net Mashiki (KMMH16)

Thickness (m)	Depth (m)	Vs (m/s)	Vp (m/s)
3	3	110	240
12	15	240	380
18	33	500	1180
8	41	400	1180
28	69	760	1950
32	101	820	2300
32	133	1470	2800
10	143	700	2800
26	169	1380	2800
32	201	840	2300
33	234	1470	2300
–	–	2700	4800

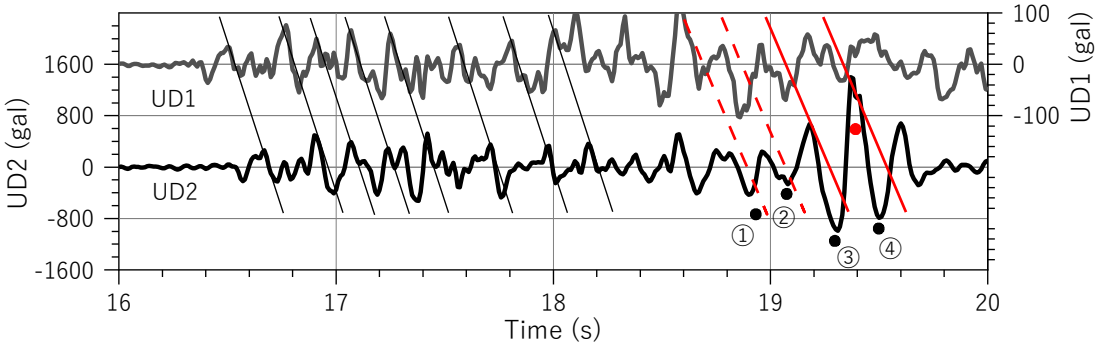

Fig. A3 Vertical acceleration time history waveforms (UD1 and UD2 components)

The ground data of KiK-Net Masaki (KMMH16) is shown in Table A2. The table indicates the shear wave velocity *Vs* = 110 m/s down to GL−3m, and up to GL−15 m, *Vs* = 240 m/s. Below that, there is an engineering bedrock with *Vs* = 500 m/s. It is believed that the surface layer is located above the groundwater level based on the P-wave velocity. The downward vertical motions (volumetric expansion) observed at positions ①–④ are considered to be a result of reversible volume changes caused by amplified shear strain in the first layer[2)–5)].

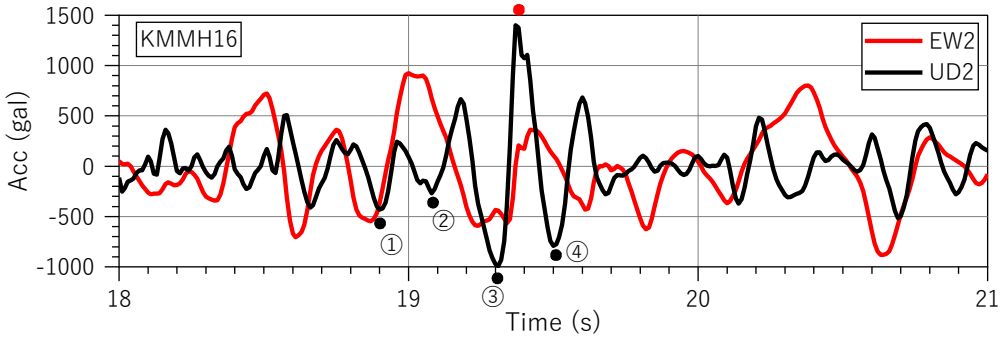

Fig. A4 Acceleration time history waveforms (UD2 and EW2 components)

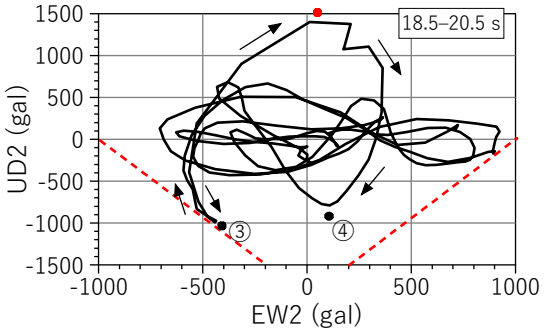

Fig. A5 Acceleration orbit (UD2 and EW2 components)

REFERENCES

1) Morio, S., Kato, Y. and Fujii, T.: Elasto-Plasticity Consideration of the Ground on the Large Acceleration Time Histories at Two Earthquake Observation Sites, *Journal of Japan Association for Earthquake Engineering*, Vol. 17, No. 4, pp.30–49, 2017 (in Japanese).
2) Murayama, S.: Constitutive Equation of Cohesionless Sand in Elastic State, *Journal of Japan Society of Civil Engineering*, No.236, pp.125–137, 1975 (in Japanese).
3) Murayama, S.: Constitutive Equation of Cohesionless Sand in Plastic State, *Journal of Japan Society of Civil Engineering*, No. 251, pp. 77–90, 1976 (in Japanese).
4) Fukutake, K. and Matsuoka, H.: A Unified Law for Dilatancy under Multi-Directional Simple Shearing, *Journal of Japan Society of Civil Engineering*, No. 412/III-12, pp. 143–151, 1989 (in Japanese).
5) Shamoto, Y., Zhang, J. M. and Goto, S.: Mechanism of Large Post-Liquefaction Deformation in Saturated Sand, *Soils and Foundations*, Vol. 37, No. 2, pp. 71–80, 1997.
6) Nakazawa, S., Sakai Y., Shiomitsu M. Miki, A. and Arai, S.: Damage Situation Around the Seismic Stations in the 2018 Hokkaido Eastern Iburi Earthquake and Correspondence of Damage to Buildings with Strong Ground Motions, *Journal of Japan Association for Earthquake Engineering*, Vol. 19, No. 7, pp.67–104, 2019 (in Japanese).
7) Morio, S. and Kato, Y.: On the Propagation Characteristics of the Seismic Wave in Kobe Port Island during the 1995 Hyogoken-Nambu Earthquake, *Bulletin of Maizuru National College of Technology*, No.38, pp. 58–73, 2003 (in Japanese).
8) Nozu, A.: Multi-Reflection Theory (2E Wave, Viscous Boundary), 2018 (in Japanese). https://www.pari.go.jp/bsh/jbn-kzo/jbn-bsi/taisin/tutorial_jpn/tutorial_015.pdf (last accessed on December 30, 2021)
9) Sato, T., Sugito, M., Kiyono, J., Sawada, S., Morio, S., Suetomi, I. and Kita, K.: 3.3.2 Study on Phase Characteristics (Time Delay) of Horizontal/Vertical Motions in Strong Earthquake Records, *Great Hanshin-Awaji Earthquake Investigation Report (Explanatory Edition)*, Japanese Geotechnical Society, Great Hanshin-Awaji Earthquake Investigation Committee, pp. 126–130, 1996 (in Japanese, title translated by the authors).
10) Satoh, T.: Analysis on Tilt and Settlement in Strong Motion Records, *Journal of Japan Association for Earthquake Engineering*, Vol. 20, No. 7, pp. 69–85, 2020 (in Japanese).
11) Hanzawa, H.: Practical Application of Soil Direct Shear Test Results, *Proceedings of the Symposium on Methods and Applications of Direct Shear Testing*, Japanese Geotechnical Society, pp. 87–94, 1995 (in Japanese, title translated by the authors).
12) Yagi, N.: Volume Change and Excess Pore Water Pressure in Sands under Repeated Shear Stress, *Journal of Japan Society of Civil Engineering*, No. 275, pp. 79–90, 1978 (in Japanese).
13) Iwamoto, I., Kokusho, T. and Nakano, T.: Volume Change Characteristics of Gravelly Sands by Means of Monotonic and Cyclic Shear Test, *Journal of Japan Society of Civil Engineering*, No. 736/III-63, pp. 205–215, 2003 (in Japanese).

14) Pradhan, T. B. S. and Tatsuoka, F.: On Stress-Dilatancy Equations of Sand Subjected to Cyclic Loading, *Soils and Foundations*, Vol. 29, No. 1, pp. 65–81, 1989.
15) Wood, D. M.: Soil Behaviour and Critical State Soil Mechanics, Cambridge University Press, 462 pp., 1990.
16) Sekiguchi, H.: Cam Clay Model, Introduction of Constitutive Equations for Soil Engineers—Seminar—, Japanese Geotechnical Society Kansai Branch, pp. 1–52, 1993 (in Japanese).
17) Asaoka, A., Sawada, Y., Noda, T., Yamada, S., Shimizu, R. and Takaine, T.: An Attempt to Replicate the So Called "Trampoline Effect" in Computational Geomechanics, *Proceedings of the Symposium on Strong Nonlinear Phenomena in Surface Soils and Their Effects during Extremely Strong Earthquakes*, Japanese Geotechnical Society Kanto Branch, pp. 47–52, 2018 (in Japanese).
18) Morio, S., Kusakabe, S., Yasufuku, N. and Hyodo, M.: A Cyclic Elasto-Plastic Constitutive Model for Sand Considering the Effect of Non-Coaxiality, *Journal of Japan Society of Civil Engineering*, No. 487/III-26, pp. 139–148, 1994 (in Japanese).
19) Shibuya, S.: Recent Developments in Direct Shear Tests on Soils and the Interpretation of Results, *Proceedings of the Symposium on Methods and Applications of Direct Shear Testing*, Japanese Geotechnical Society, pp.87–94, 1995 (in Japanese, title translated by the authors).
20) Yanagimoto, J.: Plastic Constitutive Equation (Elasto-Plasticity and Rigid-Plasticity), Institute of Industrial Science, The University of Tokyo, 11 pp. (in Japanese). https://www.cem.t.u-tokyo.ac.jp/wp-content/uploads/2023/07/adcfa4169efc91793760becea29867cd.pdf (last accessed on May 8, 2025)
21) Owen, D. R. J. and Hinton, E.: Finite Element in Plasticity—Theory and Practice, Pineridge Press Limited, Swansea, U.K., 594 pp., 1980.
22) Hashiguchi, K.: Latest Elasto-Plasticity, Asakura Publishing Co., LTD., 205 pp., 1990 (in Japanese, title translated by the authors).
23) Morio, S. and Kusakabe, S.: On the Vertical Motion Caused by Dilatancy, *Proceedings of the 52th Annual Conference of the Japan Society of Civil Engineering*, III-A117, pp. 234–235, 1997 (in Japanese).
24) Nozu, A.: Frequency Contents of Shear Stress in Ground, *35th Japan National Conference on Geotechnical Engineering*, pp. 2371–2372, 2000 (in Japanese).
25) Aoi, S., Kunugi, T. and Fujiwara, H.: Trampoline Effect in Extreme Ground Motion, *Science*, Vol. 322, pp. 727–730, 2008.
26) Technical Committee of Ground Failure and Strain Localization: *Ground Failure and Strain Localization*, The Japanese Society of Soil Mechanics and Foundation Engineering, 348 pp., 1994 (in Japanese, title translated by the authors).
27) Technical Committee of Granular Materials: *Mechanics of Granular Materials*, The Japanese Society of Soil Mechanics and Foundation Engineering, 319 pp., 1993 (in Japanese).
28) Hashiguchi, K.: New Advancement in Elastoplasticity—Concept of Subloadind Surface—, *Journal of Japan Society of Civil Engineering*, Vol. 63, No. 3, pp. 691–710, 2007 (in Japanese).
29) Morio, S., Kato, Y. and Fujii, T.: The Type of Faults, the Radiation Pattern of Earthquake Wave and Mohr's Stress Circle, *Japanese Geotechnical Journal*, Vol. 10, No. 4, pp. 611–621, 2015 (in Japanese).
30) Editing Committee for the Revision of Soil Investigation: *Japanese Geotechnical Society Standards Laboratory Testing Standards of Geomaterials*, 1st revised ed., Japanese Geotechnical Society, 1282 pp., 2009 (in Japanese).
31) Morio, S., Kusakabe, S., Yasufuku, N. and Hyodo, M.: The Evaluation of Anisotropic Sand under Undrained Conditions Based on an Elasto-Plastic Constitutive Model, *Journal of Japan Society of Civil Engineering*, No. 505/III-29, pp. 287–296, 1994 (in Japanese).
32) Tatsuoka, F. and Park, C.: Anisotropy of the Ground 4. Anisotropy of Deformation and Strength Characteristics of Sand—Anisotropy in Element Testing—, *Soil Mechanics and Foundation Engineering*, Vol. 41, No. 7, pp. 79–87, 1993 (in Japanese, title translated by the authors).
33) Schnabel, P. B., Lysmer, J. and Seed, H. B.: *SHAKE—A Computer Program for Earthquake Response Analysis of Horizontally Layered Sites*, Earthquake Engineering Research Center, EERC 72-12, 88 pp., 1972.

34) Morio, S. and Kato, Y.: On the Application of Biot's Consolidatio Theory to the Post-Liquefaction Process Involving Water Film Generation, *Bulletin of Maizuru National College of Technology*, No. 46, pp. 19–26, 2011 (in Japanese).
35) Morio, S., Kosa, K. and Miyamoto, A.: Study on Dynamic Elastic-Plastic Analysis Method for RC Rigid Frame Piers, *Proceedings of the 1st Symposium on Seismic Design of Bridges Based on Earthquake Load Bearing Capacity Method*, pp. 131–134, 1998 (in Japanese, title translated by the authors).
36) Motosaka, M.: Lessons of the 2011 Great East Japan Earthquake Focused on Characteristics of Ground Motions and Building Damages, *Proceedings of the International Symposium on Engineering Lessons Learned from 2011 Great East Japan Earthquake*, pp. 166–185, 2012.

(Original Japanese Paper Published: February, 2023)
(English Version Submitted: January 31, 2025)
(English Version Accepted: April 17, 2025)